Modelling the Fate of Mercury Emissions from Artisanal and Small Scale Gold Mining

Ian M. Hedegcock[1], Francesco De Simone[1], Francesco Carbone[1], and Nicola Pirrone[1]

[1]CNR-Institute of Atmospheric Pollution Research, 87036 Rende, Italy

Correspondence: Ian M. Hedegcock (ian.hedgecock@iia.cnr.it)

Abstract. A mercury (Hg) tracer model based on WRF-Chem has been developed to provide a rapid and relatively simple tool to evaluate the local and regional impact of Artisanal and Small Scale Gold Mining activities which use Hg amalgamation. Artisanal gold mining, its use of mercury amalgamation and its potential for human and environmental harm is mentioned specifically in the Foreword by the Secretary-General of the United Nations António Guterres of the Minamata Convention on

5   Mercury: Text and Annexes (2023 edition, url below). Much of this artisanal mining occurs in the Tropics, and often in densely forested regions and the role of vegetation in the global atmospheric mercury cycle has been shown to be significant in recent years. The model employs a simple lifetime approach to Hg^0 oxidation based on KPP and an ad hoc deposition scheme which calculates the foliar uptake of $Hg^0_{(g)}$ based on the Leaf Area Index, dry deposition of $Hg^{II}_{(g)}$, and the wet deposition of $Hg^{II}_{(g)}$ by convective and non-convective precipitation. A number of demonstration simulations are presented using four example do-

10   mains from South-East Asia and South America, and five from Africa. The results highlight the diversity of the local impacts of ASGM due to land category, geography and meteorology, but also point to the fact that just as there are always local impacts there are also repercussions for the global atmospheric mercury burden.
(https://minamataconvention.org/sites/default/files/documents/information_document/Minamata-Convention-booklet-Oct2023-EN.pdf)

1   Introduction

1.1   Artisanal and Small Scale Gold Mining

To quote the Secretary-General of the United Nations, António Guterres,

"*Like so many contaminants, mercury doesn't just damage individual victims. It damages entire communities. It fuels poverty, feeds conflict and pushes equality further out of reach. Take the example of a young mother working as an artisanal gold miner.*

20   *While she is poisoned from handling mercury at work, countless others, including her children, are harmed by its impact on the environment.*

The Minamata Convention is our chance to break that cycle of misery. (United Nations, 2023)

ASGM is currently the major anthropogenic atmospheric source of Hg to the atmosphere, having overtaken coal fired power
25 generation, according to the latest Global Mercury Assessment (GMA) by the United Nations Environment Program (UNEP)
(UN-Environment, 2019). The Minamata Convention on Mercury (https://minamataconvention.org/en) is a global treaty with
the stated intention of "*protecting human health and the environment from the adverse effects of mercury*". Nations which are
signatories to the convention are required to address mercury mining, its use, import/export, storage and eventual disposal as
waste, among the numerous obligations contained in the convention. Article 7 of the Convention explicitly addresses ASGM,
30 and requires parties to "*take steps to reduce and where possible eliminate the use of Hg and its emission and release to the
environment, from such mining and processing*". Much ASGM takes place in tropical regions and consequently in areas which
are often densely vegetated.

1.2   Vegetation in the atmospheric Hg cycle

Recent studies have highlighted the importance of vegetation in the atmospheric cycle of Hg (Jiskra et al., 2018; Zhou et al.,
35 2021; Zhou and Obrist, 2021; Feinberg et al., 2022).

Inputs of Hg from litterfall have been estimated to be as great as $1000 \, \mathrm{Mg}$ a year (Wang et al., 2016), see Feinberg et al.
(2022) for a recent compilation of Hg litterfall, throughfall and dry deposition measurements. Hg input to forest ecosystems is
currently being studied in different types of forests in a numerous locations in order to constrain this sink for atmospheric Hg
(e.g. Wright et al. (2016); Zhou et al. (2018b); Risch and Kenski (2018); Li et al. (2022); Huang et al. (2023); Méndez-López
40 et al. (2023).

As pointed out by Obrist et al. (2021) Hg entering the forest ecosystem can enter runoff, be bioaccumulated in aquatic
ecosystems and eventually pose a risk of exposure to terrestrial wildlife, including humans. In many regions this deposition
pathway will clearly have a seasonal cycle as demonstrated by Jiskra et al. (2018).

The Leaf Area Index (LAI, $\mathrm{m^2 \, m^{-2}}$) is a measure of the total one-sided leaf area per unit ground area, or "*leafiness*". As the
45 uptake of Hg by vegetation is proportional to leaf area, and LAI is highest in the Tropics and sub-Tropics where much of the
world's ASGM occurs, it is natural to ask how much of the Hg released from ASGM is deposited in the local ecosystem and
how much will join the global atmospheric Hg pool. A recent study by Gerson et al. (2022) shows that undisturbed forest is a
significant sink for Hg released from ASGM in the Amazon.

1.3   Modelling

50 A conceptually simple Hg tracer mechanism has been implemented in the regional atmospheric chemical transport model
(CTM) has been developed based on WRF-Chem (Grell et al., 2005) to investigate the fate of Hg emitted from ASGM. The
model uses a parametrised approaches to Hg^0 uptake by vegetation, Hg^0 oxidation in the atmosphere, and the wet deposition
of Hg^{II} produced by oxidation.

Given the frequency and intensity of rainfall in the Tropics and the sub-Tropics means that scavenging and wet deposition is
55 likely to provide another significant deposition pathway for the Hg released by ASGM.

This study describes a modelling tool which estimates the Hg deposition/uptake due to the Hg emissions from a given area in which ASGM occurs. The model is designed to be relatively simple to use for anyone with a little experience of Numerical Weather Prediction (NWP) or climate models.

The examples shown here choose a supra-continental modelling domain, with nested domains to focus on the areas of interest, and after running the meteorological preprocessor, the Hg emissions are assigned to the appropriate nested domains, after which the model is run for a year. The results currently distinguish between deposition via vegetation uptake, convective and non-convective wet, and dry deposition. The model, due to its parametrised approach runs more quickly than a CTM with full chemistry and potentially could be used in conjunction with policy makers or NGOs to provide a rapid assessment, using local knowledge, of the probable impact of individual mining sites/areas on neighbouring communities, agricultural land, waterbodies and ecosystems.

2 Methodology

2.1 The WRF-model & Chemistry

The KPP version of WRF-Chem (Damian et al., 2002; Sandu and Sander, 2006; Salzmann and Lawrence, 2006; Salzmann, 2008) has been used to add tagged Hg tracer chemical mechanisms to the WRF-Chem model Grell et al. (2005), WRF version 4.3 Skamarock et al. (2019) was used in this study. Each mechanism is domain specific and includes a number of Hg tracer species for the individual ASGM emission source regions, in order to follow their fate. The Hg tracers have lifetimes of 180, 270 and 360 days, which is implemented by simply including a reaction in the KPP mechanism which produces an oxidised Hg tracer (Hg^{II}, also tagged according the emission source of the Hg) at a rate proportional to the lifetime. The tracers also have three different vegetation uptake rates, see 2.2.1, so that there are 9 tracer species with different lifetime and deposition characteristics for each emission source region. The use of lifetimes for Hg^0 oxidation provides a simple (and computationally efficient) approach to the problem of the complex, and as yet, not fully determined redox chemistry of atmospheric Hg . The wealth of monitoring data now available does however permit upper and lower limits on its atmospheric lifetime, even if the complexities of Hg redox chemistry are still being uncovered, see for example, (Saiz-Lopez et al., 2019; Shah et al., 2021; Castro et al., 2022), although polar regions appear to be better understood (Araujo et al., 2022; Dastoor et al., 2022).

2.1.1 Domains and Emissions

The domains have been chosen to be representative three important ASGM regions in the Tropics, namely, South-East Asia, Africa and South America. The large outer domain is supra-continental (216 km resolution) in order to obtain some idea of emission transport beyond the regional scale. Within this domain there is a second domain at 72 km resolution, within which, four, or in the case of the African modelling domain, 5, smaller domains at 24 km resolution. The small domains serve primarily to confine the AGSM to a relatively small area for tagging purposes. The smallest domains were chosen with a view to trying to use areas with different geographical and ecosystem features in each simulation, with the caveat that the choice of source

region was governed by the presence of ASGM activity. The domains include a number of types of mining localities, ranging from densely forested tropical areas, savannah woodland, savannah scrub to semi-arid areas, and include island, coastal and inland sites, see figure 1.

90   The emissions used in this study are from EDGARv4.tox2 Muntean et al. (2018), as it is simple to use with WRF-Chem in conjunction with the *anthro_emis* preprocessor https://www2.acom.ucar.edu/wrf-chem/wrf-chem-tools-community and has the resolution necessary to identify relatively localised mining areas. The emissions from each of the domains for the individual mining regions were tagged using *anthro_emis*, and had a series of tracer emissions reflecting the 9 combinations of atmospheric lifetime and rate of deposition to vegetation described above. It should be pointed out that the emissions from

95   EDGARv4.tox2 used in this study refer to the year 2012 and should not necessarily be considered representative of current ASGM Hg emissions.

Using the EDGAR database the resolution could be reduced to 10-12 km in tropical areas as the database horizontal spatial resolution is $0.1°$ by$0.1°$. However, with more detailed local, ground based knowledge of the location of sites, and especially Hg use and amalgamation methods, the emissions could be far better constrained in specific locations than they are in global

100   databases (Bruno et al., 2023), and would give a more precise idea of the impact on local vegetation and cultivation.

2.1.2   Meteorology

The model uses meteorological data from the NCEP FNL Operational Model Global Tropospheric Analyses (National Centers for Environmental Prediction, National Weather Service, NOAA, U.S. Department of Commerce, 2000), and was run from the beginning of December 2017 until the end of December 2018. The first month is spin-up, and the analysis is for January -

105   December 2018.

2.2   Hg uptake by vegetation

The role that vegetation plays in determining the terrestrial-atmospheric flux of Hg has become more and more clear over the last few years. The seasonal variation in Northern Hemisphere atmospheric Hg concentrations, when compared to the relative stability of that in the Southern Hemisphere led Jiskra et al. (2018) to propose a fundamental role for vegetative uptake of $Hg^0_{(g)}$,

110   which varied with the seasonal rhythm of plant growth. Further studies have since confirmed the importance of vegetation in the atmospheric Hg cycle (Jiskra et al., 2018; Zhou et al., 2021; Zhou and Obrist, 2021), although the magnitude of the atmosphere to biosphere flux is not, as yet, very well constrained, see (Feinberg et al., 2022).

In part this uncertainty stems from a paucity of detailed studies on the way different plant species (trees, shrubs, grasses, mosses, lichens etc) take up Hg from the atmosphere, and how the uptake changes over the seasons. It is important however, to

115   distinguish between "total deposition flux via vegetation" and uptake from the atmosphere by vegetation. Annual atmospheric Hg uptake by vegetation has been estimated to be between 1000 (Jiskra et al., 2018) (during the vegetation period, the authors point out that gross uptake may well be greater), 2422 (Zhou and Obrist, 2021), and recently 2276 $\mathrm{Mg\,yr^{-1}}$ (Feinberg et al., 2022). In another recent paper total Hg assimilation by all plant functional types was estimated to be 2377 $\mathrm{Mg\,yr^{-1}}$ Yuan et al. (2023). The estimate by Zhou and Obrist (2021) specifically regards the deposition to above ground plant tissues, and the

authors point out that the total deposition flux via vegetation (including throughfall, Hg assimilated and transported to plant root systems, and plant turnover) could be over $4000 \, \mathrm{Mg \, yr^{-1}}$, taking into account both Hg^{II} and Hg^0.

Mercury isotope studies are giving further insights into the processes involved in atmosphere- vegetation Hg exchange (see Tsui et al. (2020); Wang et al. (2022); Chen et al. (2023) and references therein). This level of detail is beyond the simplified modelling approach used here. Studies of how stomatal processes influence Hg^0 uptake are also improving understanding of the global vegetation sink (Wohlgemuth et al., 2022; Yuan et al., 2023), again this level of detail goes beyond the intentions of this study.

How stressors such as rising temperatures, changing rainfall patterns, land use change will affect this sink of atmospheric Hg is as yet unclear, but as pointed out by Feinberg et al. (2022) and Sonke et al. (2023) it is important; as Hg not taken up by plants can be deposited to the ocean where it can enter the food chain. As is well known by now, human exposure to Hg is predominantly through the consumption of piscivorous fish species such as tuna (UN-Environment, 2019).

2.2.1 Parametrisation of uptake by vegetation

The global average LAI ranges from 1.98 to $2.31 \, \mathrm{m^2 \, m^{-2}}$ (Fang et al., 2019), and the earth's land surface covers 148,940,000 $\mathrm{km^2}$, hence the global leaf area is of the order of $\approx 2.95 - 3.44 \times 10^{14} \, \mathrm{m^2}$. Annual atmospheric Hg uptake by vegetation has been estimated to be between 1000 (Jiskra et al., 2018) and 2422 (Zhou and Obrist, 2021) $\mathrm{Mg \, yr^{-1}}$, these are the lowest and highest estimates, see section 2.2.

For the purpose of this model it is possible to derive a range of feasible rates of Hg^0 uptake in terms of leaf area. It has been assumed that 100% of emissions to the atmosphere from ASGM are Hg^0 as in the emissions database. Using the highest global average LAI with the lowest Hg^0 annual uptake estimate gives an uptake rate of $2.9 \, \mathrm{\mu g \, m^{-2} \, yr^{-1}}$, while the lower average LAI and the higher uptake estimate gives an uptake rate of $8.2 \, \mathrm{\mu g \, m^{-2} \, yr^{-1}}$.

In the model three rates have been used, the upper and lower estimates and a value between the two. In the model itself, values of 9.22×10^{-5}, 1.78 and $2.63 \times 10^{-4} \mathrm{ng \, m^{-2} \, s^{-1}}$ have been used. This value is then divided by a given background concentration of Hg^0, $1.4 \, \mathrm{ng \, m^{-3}}$ in this case. Doing this provides leaf area dependent deposition velocities of 6.58×10^{-5}, 1.27 and $1.88 \times 10^{-4} \mathrm{m \, s^{-1}}$, and the actual deposition velocity is obtained by multiplying these by the LAI of the given model cell. The time varying LAI values are provided as model input via the WRF preprocessing system (WPS).

Vegetation uptake is only considered in the first model layer. In these simulations the first model layer has a depth of $\approx 50\mathrm{m}$, and varies by less than 2m over the domain. Global canopy height studies suggest that with the exception of a very few areas mean canopy height rarely exceeds $50 \, \mathrm{m}$, (Lang et al., 2022; Potapov et al., 2021).

2.3 Precipitation and Scavenging ratio

The scavenging ratio, the ratio of a substance (Barrie, 1985; Cheng et al., 2021), concentration in precipitation to its concentration in air, has been estimated for Hg in relatively few studies (Sakata and Asakura, 2007; Seo et al., 2012; Huang et al., 2013; Zhou et al., 2018a), however the values obtained are fairly consistent for Hg^{II} and a value of $750 \, \mathrm{m^3_{rain} \, m^{-3}_{air}}$ Seo et al. (2012); Zhou et al. (2018a), been used here. Typically units are $\mathrm{\mu g \, L^{-1}}$ for the concentration in precipitation and $\mathrm{\mu g \, m^{-3}}$, in

the model $\mathrm{ng\,L^{-1}}$ and $\mathrm{ng\,m^{-3}}$ have been used, for consistency with the usual mode of expression of Hg concentrations. Wet deposition is triggered if the time step rainfall is above a given threshold (currently $0.4\mathrm{mm\,h^{-1}}$, moderate drizzle).

155   The WRF model distinguishes between convective and non-convective rainfall and therefore the distinction has been maintained in the Hg deposition output.

The model loops over the atmospheric column and calculates the average Hg^{II} concentration, up to $\approx 4000\mathrm{m}$ (600hPa) in the case of non-convective rain, $\approx 12000\mathrm{m}$ (180hPa) for convective precipitation. This value is used to calculate the concentration of Hg^{II} in the precipitation which reaches the ground, and the concentration of Hg^{II} is then recalculated taking into

160   account the amount lost via precipitation.

2.4 Dry deposition

The fraction of $\mathrm{Hg}^0_{(g)}$ converted to $\mathrm{Hg}^{II}_{(g)}$ is subject to a simple dry deposition parametrisation in which a model wide deposition velocity is chosen and applied to a set number of model layers. This approach simplifies the calculation of the deposition velocity. Velocities of $1\,\mathrm{cm\,s^{-1}}$ and $2\,\mathrm{cm\,s^{-1}}$ were used, and applied to the first and the first two model layers respectively to

165   assess the influence this had on the overall deposition and the partitioning of the deposition into the four categories, vegetation uptake, convective and non-convective wet deposition and dry deposition.

3   Results and Discussion

3.1   Deposition within the modelling domain

The large scale regional impact can be determined simply by looking at the fraction of total ASGM emissions that remain in

170   the largest modelling domain. Looking at the simulation results which use the slowest and fastest oxidation rates and the least and most rapid uptake of $\mathrm{Hg}^0_{(g)}$, the percentage of emissions which remain within the largest modelling domain ranges from around 6 to almost 80%, as can be seen in tables 2 to 4. With the exception of the Kalimantan emission domain, the in-domain deposition is between 10 and 25% in almost all cases, where it less (italics) or greater (bold) the entries have been highlighted in the tables. That a large fraction of the Hg emissions are deposited outside the modelling domain, or travel beyond the domain

175   to be deposited in it again after circling the globe, is not surprising given that it well known that Hg is a global pollutant (UN-Environment, 2019). Dry deposition (the combination of foliar uptake of $\mathrm{Hg}^0_{(g)}$ and the deposition of $\mathrm{Hg}^{II}_{(g)}$ is greater than wet deposition in all but very few cases, highlighted in red in the table. Non-convective wet deposition is to all extents and purposes irrelevant when compared to convective wet deposition. Foliar uptake of $\mathrm{Hg}^0_{(g)}$, on the other hand, is the consistently the major Hg sink with only a few exceptions, highlighted in blue in tables 2 to 4.

180   That dry deposition predominates over wet deposition in all the simulated scenarios, apart from the three highlighted in red in tables 2 to 4 is due in great part to the emissions from ASGM being all $\mathrm{Hg}^0_{(g)}$, and emitted into the first model layer. Oxidation to Hg^{II} (weeks/months) is relatively slow compared to horizontal transport, air circumnavigates the globe in a matter of weeks, and takes around a week to reach the free troposphere (see Jacob (1999) for example). Therefore the fraction of Hg^0

emitted from ASGM, subsequently oxidised and deposited by precipitation within the domain is generally small compared to the fraction deposited via foliar uptake or dry deposition. The determining factor on how large a fraction of the Hg^0 emitted is deposited within the domain is the foliar uptake rate rather than the oxidation rate, as is clear from tables 2 to 4, where it can be seen that the fast foliar uptake rate roughly doubles the in-domain deposition, for the emission domains which are more highly vegetated, such as Brazil and Kalimantan. The difference is less for those domains with emissions in mountainous, such as Colombia and Bolivia and less densely vegetated regions like Sudan and Burkina Faso.

3.1.1 The dry deposition velocity of $Hg_{(g)}^{II}$

As mentioned in section 2.4, simulations were performed using $Hg_{(g)}^{II}$ dry deposition velocities of $1\,\mathrm{cm\,s^{-1}}$ for the lowest model layer and $2\,\mathrm{cm\,s^{-1}}$ for the lowest two model layers. Comparison of the results from these pairs of simulations are shown in tables A1, A2 and A3. Note that the percentage of $Hg_{(g)}^{II}$ dry deposition is the percentage of the total emissions during the simulation period.

A noticeable difference in the change in $Hg_{(g)}^{II}$ dry deposition can be seen in tables A1 to A3. Whereas in both the South American and African simulations the increase in v_d leads to a roughly 50 – 55% increase in dry deposition of $Hg_{(g)}^{II}$, in the South-East Asia simulations the increase in v_d leads to a more than 100% in $Hg_{(g)}^{II}$ dry deposition. in the case of the Mekong region and Sumatra it is between 100 and 120%, but for Kalimantan and Papua New Guinea it is around 160%.

The impact that this has on total in-domain deposition is of course less, as there are four different Hg deposition pathways, and foliar uptake and convective deposition of Hg^{II} are the predominant pathways. Nonetheless, the in domain deposition increase is almost 10% in some cases in the South American and African domains, although generally closer to 5%, while it is generally around 10% for the South-East Asian domains with highs of 17 and 21% in Papua New Guinea and Kalimantan.

Why South-East Asia should be different from the other two regions is interesting. It is possibly due to the Borneo Vortex, which is a quasi-stationary cyclonic weather system generally centred between the northern coast of Borneo and the eastern coast of peninsular Malaysia, see for example Liang et al. (2021, 2023) and references therein. These systems occur in boreal winter and would inhibit atmospheric transport out of the modelling domain while they last. However, such a detailed investigation to ascertain the reason for the difference seen in the South-East Asian domain is beyond the scope of this study. However, it is clear that the prevailing weather and characteristic atmospheric transport from emission regions will clearly play a part in determining the details of the dispersion and deposition of emitted Hg from ASGM sites. Some general characteristics of the local vs. regional deposition for the different deposition pathways are discussed and illustrated below, as it is important for the communities in and around areas where mining occurs to understand how much of the in-domain deposition occurs locally and could potentially affect their wellbeing.

3.2 Deposition distance distribution

The deposition distribution from the different ASGM regions is not homogeneous within the domain, which is in part due to their geographical location and also due the type of terrain and vegetation in the local vicinity. Figure 2 shows the smallest modelling domain for the South American simulations with the emissions overlaid on a high resolution topographic relief map

((NOAA National Geophysical Data Center, 2009; Amante and Eakins, 2009), the SE Asian and African domains can be found in the Supplementary Information, section S1 figures S1 and S2.

The prevailing wind direction, distance from the coast, the type and density of the surrounding vegetation, and the local orography all play a role in determining the distribution of Hg deposition. The plots in Figure 3, 4 and 5 show the distribution of Hg deposition as a function of distance from the centre of the smallest modelling domains where the emissions occur. Note that the y-axes (deposition) are logarithmic. Each of the smallest modelling domains is approximately $10°$ by $10°$, which at the equator is roughly $1100\,\mathrm{km}$ by $1100\,\mathrm{km}$, therefore any distance less than $500\,\mathrm{km}$ is effectively within the smallest modelling domain. These figures show the results from the simulations with the slowest oxidation rate and slowest foliar uptake rate. The figures illustrating the results from the fastest oxidation rate and fastest foliar uptake are in the Supplementary Information, figures S3, S4 and S5. All the figures below and those in the Supplementary Information show the results from the simulations assuming an $\mathrm{Hg}_{(g)}^{II}$ deposition velocity of $1\,\mathrm{cm\,s}^{-1}$.

The foliar uptake fluxes can be seen to generally fall away rapidly with distance from the emission source, and the same is true of dry deposition. The Hg deposition via precipitation pathways shows a less pronounced diminution close to the source. In order for the Hg^0 emissions from ASGM to be deposited via precipitation pathways requires both oxidation to $\mathrm{Hg}_{(g)}^{II}$ as well as the presence of rain, hence it is not surprising that the deposition via precipitation is less localised than the foliar uptake and dry deposition of Hg. Dry deposition of $\mathrm{Hg}_{(g)}^{II}$ competes in a sense with the precipitation deposition pathways as locally produced $\mathrm{Hg}_{(g)}^{II}$ is likely to be relatively rapidly deposited, further adding to the '*delocalistion*' of the precipitation deposition.

However, while the deposition - distance plots, Figures 3 - 5 show how deposition fluxes vary with distance, the use of the a logarithmic scale for the deposition axis, slightly obfuscates how much and how close (or far) the deposition is from the emission source.

Figures 6 - 9 divide each deposition pathway into distance bins and the percentage of the total deposition (within the modelling domain) is shown. In these bar charts the percentages are referred to the total deposition of each individual deposition pathway deposited within the modelling domain (the sum of each of the bars is therefore 100%). As can be seen in the figure captions these figures show the results from the simulations where $v_d=1\,\mathrm{cm\,s}^{-1}$, the results for $v_d=2\,\mathrm{cm\,s}^{-1}$ are shown in figures S6 - S8 in the Supplementary Information. Comparing figures 6 - 9 and S6 - S8 the similarity between the charts is clear, showing that the dry deposition velocity of $\mathrm{Hg}_{(g)}^{II}$ (and whether it is considered in the first, or the first two levels), does not have a major influence on the modelling results. In most cases between 20 and 60% of the foliar uptake, occurs locally, and generally speaking from 10 to 30% of the total in domain deposition is local. There are some exceptions to this however, as discussed in the following sections.

3.2.1 South East Asia

There is a noticeable difference between all the other dry deposition plots and those for Kalimantan and Papua New Guinea. This would appear to support the suspicion that transport away from these regions is slower than for the other regions, at least for part of the time possibly due to the Borneo Vortex, as discussed above in section 3.1.1. As discussed in section 3.1.1 the value of v_d makes the greatest difference in this region, and increases overall in domain deposition by $\approx 10\%$, for the Mekong and

Sumatran, and 17 and 21% for the Papua New Guinea and Kalimantan domains respectively. However, given the predominance of foliar uptake in the total in domain deposition, the deposition distance distributions do not change qualitatively. The maps of deposition in this domain also illustrate the difference in foliar uptake and dry deposition between the Kalimantan and Papua New Guinea emission regions compared to the Mekong and Sumatra domains, see figures S9 - S12. The bar charts in figure 6 show the major part of Hg foliar uptake, dry deposition and total deposition of the emissions from the Kalimantan and Papua New Guinea domains occurs within a radius of 1000 and 500 km respectively. This pattern is different from the other South-East Asian emission domains as well as different from the South American and African emission domains. The maps of deposition in this domain also illustrate

3.2.2 South America

The foliar uptake of Hg falls away rapidly with distance as can be seen in both the scatter plots and barcharts (figures 3 and 7. Guyana and Bolivia show high foliar uptake and total deposition within 500 km of the emission source, but within this area the contribution from dry deposition of Hg is significantly lower than seen for the Kalimantan and Papua New Guinea domains. Dry deposition tends to peak in conjunction with the wet precipitation peaks as would be expected if transport from the source region is relatively rapid and oxidation of Hg occurs during transport. The maps of the individual deposition pathways can be found in figures S13 - S16

3.2.3 Africa

The situation for the African domains differs again, and the most noticeable difference is the part of the foliar uptake which occurs 000's of km from the emission regions. In the cases of Burkina Faso, Sudan and Senegal the 50% or more of the foliar uptake of Hg occurs more than 2000 km away from the ASGM source. This occurs due to a combination of the nature of the local vegetation, which in a number of cases is very scarce or scrubland, the direction of the prevailing winds, and in the case of West Africa, the vicinity of the Atlantic Ocean. This leads to the gaps in the foliar uptake plots which are particularly apparent in the plots of emission sources from West Africa (figure 5) can also be seen in Table 5 most evidently in the case of Senegal. In the foliar deposition map shown in figure 8 the westerly transport of the emissions and the foliar uptake in South America are evident. Even the emissions from the Lake Victoria and Sudanese ASGM regions result in foliar uptake of Hg in South America. The emission region which has least influence in this respect is Ghana, due to the denser vegetation near the emission source, see figure 9. Senegal, Sudan and Burkina Faso differ from all the other domains, including those in South-East Asia and South America, in that the highest proportion of the total deposition from these emission regions occurs more than 5000 km, from the source, see the deposition maps in figures S17 - S21

3.3 Potential improvements

The most important improvement that could be made is the updating of the ASGM emissions database. For individual countries or regions this could be based on local knowledge of the Hg trade, gold production method and scale, as well as the precise

geographical location of where amalgamation and amalgam refining are occurring. These details combined with a higher model spatial resolution would give a more detailed picture of the local fate of Hg emissions from ASGM sites.

The importance of LAI on the foliar uptake of Hg is by now clear, but improvements could be made in estimating the full
285   potential of ecosystems to take up Hg. Zhou and Obrist (2021) point out that lichens and mosses are not included in calculations of vegetative uptake, and in this study the use of the LAI value from the model input data does not include their contribution. Another potential source of underestimation of Hg uptake by vegetation is that the LAI of the understory is often too complex to be included in LAI estimations. As George et al. (2021) point out, satellite retrievals can provide good time dependent estimates over overstory but the understory is often ignored in ecological studies. They find that understory LAI increased with
290   species richness, which could be an important factor in tropical forest sites where ASGM occurs, although admittedly their study area only covered Europe (George et al., 2021).

4   Conclusions

This article presents the changes made to the WRF-Chem model to simply and rapidly estimate the local and regional deposition of Hg resulting from ASGM activities. This could provide valuable information to local agencies in order to provide
295   information to local communities on the possibility of agricultural or wild produce containing harmful levels of Hg. It could also provide an impetus to miners to reconsider their gold refining techniques in order to reduce the potential for contamination of their own lands and agricultural produce. The comparison of the different ASGM regions in this study highlight the importance of treating each area as an individual case as even sites that are relatively geographically close can be impacted very differently from mining activities. The model results also show that while Hg use in ASGM is inevitably a problem at a
300   local level, it has significant repercussions for the regional and global Hg burden.

Code availability. An explanation of the code changes required to produce this tracer version of the WRF-Chem model can be found in Appendix B. Examples of the changes to the KPP input files and the WRF-Chem file *'registry.chem'* are provided. The new subroutine to calculate the foliar uptake, non-convective and convective wet deposition and dry deposition is reproduced in full in the Supplementary Information, section S5.

305   *Author contributions.* Concept: NP, IMH. Experimental design: IMH, NP, FDS. Model programming: IMH. Programming/scripting for analysis and graphics: FDS, FC, IMH. Financial resources/support: NP. Ms Preparation: IMH. Ms editing FC, FDS, NP, IMH.

Competing interests. The authors declare no competing interests

Acknowledgements. We acknowledge the use of the WRF-Chem preprocessor tool anthro_emis provided by the Atmospheric Chemistry Observations and Modeling Lab (ACOM) of NCAR. www2.acom.ucar.edu/wrf-chem/wrf-chem-tools-community. Input data for WRF is provided by National Centers for Environmental Prediction, National Weather Service, NOAA, U.S. Department of Commerce (https://doi.org/10.5065/D6M043C6).

The authors acknowledge the financial contribution of the EU projects e-Shape (contract no.820852) and iGOSP (contract no. 689443).

References

Amante, C. and Eakins, B. W.: ETOPO1 1 Arc-Minute Global Relief Model: Procedures, Data Sources and Analysis. NOAA Technical Memorandum NESDIS NGDC-24, Tech. rep., National Geophysical Data Center, NOAA., https://doi.org/doi:10.7289/V5C8276M, last access: 20 March 2024, 2009.

Araujo, B. F., Osterwalder, S., Szponar, N., Lee, D., Petrova, M. V., Pernov, J. B., Ahmed, S., Heimbürger-Boavida, L.-E., Laffont, L., Teisserenc, R., Tananaev, N., Nordstrom, C., Magand, O., Stupple, G., Skov, H., Steffen, A., Bergquist, B., Pfaffhuber, K. A., Thomas, J. L., Scheper, S., Petäjä, T., Dommergue, A., and Sonke, J. E.: Mercury isotope evidence for Arctic summertime re-emission of mercury from the cryosphere, Nature Communications, 13, 4956, https://doi.org/10.1038/s41467-022-32440-8, 2022.

Barrie, L. A.: Scavenging ratios, wet deposition, and in-cloud oxidation: An application to the oxides of sulphur and nitrogen, J. Geophys. Res.,, 90(D3), 5789–5799, https://doi.org/10.1029/jd090id03p05789, 1985.

Bruno, D. E., De Simone, F., Cinnirella, S., Hedgecock, I. M., D'Amore, F., and Pirrone, N.: Reducing Mercury Emission Uncertainty from Artisanal and Small-Scale Gold Mining Using Bootstrap Confidence Intervals An Assessment of Emission Reduction Scenarios, Atmosphere, 14, https://doi.org/10.3390/atmos14010062, 2023.

Castro, P. J., Kellö, V., Cernušák, I., and Dibble, T. S.: Together, Not Separately, OH and O3 Oxidize Hg(0) to Hg(II) in the Atmosphere, J. Phys. Chem. A, 126, 8266–8279, https://doi.org/10.1021/acs.jpca.2c04364, 2022.

Chen, C., Huang, J.-H., Li, K., Osterwalder, S., Yang, C., Waldner, P., Zhang, H., Fu, X., and Feng, X.: Isotopic Characterization of Mercury Atmosphere-Foliage and Atmosphere-Soil Exchange in a Swiss Subalpine Coniferous Forest, Environ. Sci. Technol., 57, 15 892–15 903, https://doi.org/10.1021/acs.est.3c03576, 2023.

Cheng, I., Mamun, A. A., and Zhang, L.: A synthesis review on atmospheric wet deposition of particulate elements: scavenging ratios, solubility, and flux measurements, Environmental Reviews, 29, 340–353, https://doi.org/10.1139/er-2020-0118, 2021.

Damian, V., Sandu, A., Damian, M., Potra, F., and Carmichael, G. R.: The kinetic preprocessor KPP, a software environment for solving chemical kinetics, Computers and Chemical Enginerring, 26, 1567–1579, https://doi.org/10.1016/s0098-1354(02)00128-x, 2002.

Dastoor, A., Angot, H., Bieser, J., Christensen, J. H., Douglas, T. A., Heimbürger-Boavida, L.-E., Jiskra, M., Mason, R. P., McLagan, D. S., Obrist, D., Outridge, P. M., Petrova, M. V., Ryjkov, A., St. Pierre, K. A., Schartup, A. T., Soerensen, A. L., Toyota, K., Travnikov, O., Wilson, S. J., and Zdanowicz, C.: Arctic mercury cycling, Nature Reviews Earth & Environment, 3, 270–286, https://doi.org/10.1038/s43017-022-00269-w, 2022.

Fang, H., Baret, F., Plummer, S., and Schaepman-Strub, G.: An Overview of Global Leaf Area Index (LAI): Methods, Products, Validation, and Applications, Reviews of Geophysics, 57, 739–799, https://doi.org/10.1029/2018RG000608, 2019.

Feinberg, A., Dlamini, T., Jiskra, M., Shah, V., and Selin, N. E.: Evaluating atmospheric mercury (Hg) uptake by vegetation in a chemistry-transport model, Environ. Sci.: Processes Impacts, 24, 1303–1318, https://doi.org/10.1039/D2EM00032F, 2022.

George, J.-P., Yang, W., Kobayashi, H., Biermann, T., Carrara, A., Cremonese, E., Cuntz, M., Fares, S., Gerosa, G., Grünwald, T., Hase, N., Heliasz, M., Ibrom, A., Knohl, A., Kruijt, B., Lange, H., Limousin, J.-M., Loustau, D., Lukeš, P., Marzuoli, R., Mölder, M., Montagnani, L., Neirynck, J., Peichl, M., Rebmann, C., Schmidt, M., Serrano, F. R. L., Soudani, K., Vincke, C., and Pisek, J.: Method comparison of indirect assessments of understory leaf area index (LAIu): A case study across the extended network of ICOS forest ecosystem sites in Europe, Ecological Indicators, 128, 107 841, https://doi.org/10.1016/j.ecolind.2021.107841, 2021.

Gerson, J. R., Szponar, N., Zambrano, A. A., Bergquist, B., Broadbent, E., Driscoll, C. T., Erkenswick, G., Evers, D. C., Fernandez, L. E., Hsu-Kim, H., Inga, G., Lansdale, K. N., Marchese, M. J., Martinez, A., Moore, C., Pan, W. K., Purizaca, R. P., Sánchez, V., Silman, M.,

Ury, E. A., Vega, C., Watsa, M., and Bernhardt, E. S.: Amazon forests capture high levels of atmospheric mercury pollution from artisanal
350   gold mining, Nature Communications, 13, 559, https://doi.org/10.1038/s41467-022-27997-3, 2022.

Grell, G. A., Peckham, S. E., Schmitz, R., McKeen, S. A., Frost, G., Skamarock, W. C., and Eder, B.: Fully coupled "online" chemistry
within the WRF model, Atmospheric Environment, 39, 6957–6975, https://doi.org/10.1016/j.atmosenv.2005.04.027, 2005.

Huang, J., Chang, F.-C., Wang, S., Han, Y.-J., Castro, M., Miller, E., and Holsen, T. M.: Mercury wet deposition in the eastern United States:
characteristics and scavenging ratios, Environmental Science: Processes & Impacts, 15, 2321, https://doi.org/10.1039/c3em00454f, 2013.

355   Huang, J.-H., Berg, B., Chen, C., Thimonier, A., Schmitt, M., Osterwalder, S., Alewell, C., Rinklebe, J., and Feng, X.: Predominant con-
tributions through lichen and fine litter to litterfall mercury deposition in a subalpine forest, Environmental Research, 229, 116 005,
https://doi.org/10.1016/j.envres.2023.116005, 2023.

Jacob, D. J.: Introduction to Atmospheric Chemistry, Princeton University Press, http://www.jstor.org/stable/j.ctt7t8hg, 1999.

Jiskra, M., Sonke, J. E., Obrist, D., Bieser, J., Ebinghaus, R., Myhre, C. L., Pfaffhuber, K. A., Wängberg, I., Kyllönen, K., Worthy, D.,
360   Martin, L. G., Labuschagne, C., Mkololo, T., Ramonet, M., Magand, O., and Dommergue, A.: A vegetation control on seasonal variations
in global atmospheric mercury concentrations, Nature Geoscience, 11, 244–250, https://doi.org/10.1038/s41561-018-0078-8, 2018.

Lang, N., Kalischek, N., Armston, J., Schindler, K., Dubayah, R., and Wegner, J. D.: Global canopy height regression and
uncertainty estimation from GEDI LIDAR waveforms with deep ensembles, Remote Sensing of Environment, 268, 112 760,
https://doi.org/10.1016/j.rse.2021.112760, 2022.

365   Li, X., Wang, X., Yuan, W., Lu, Z., and Wang, D.: Increase of litterfall mercury input and sequestration during decomposition with a montane
elevation in Southwest China, Environmental Pollution, 292, 118 449, https://doi.org/10.1016/j.envpol.2021.118449, 2022.

Liang, J., Catto, J. L., Hawcroft, M., Hodges, K. I., Tan, M. L., and Haywood, J. M.: Climatology of Borneo Vortices in the HadGEM3-GC3.1
General Circulation Model, Journal of Climate, 34, 3401–3419, https://doi.org/10.1175/JCLI-D-20-0604.1, 2021.

Liang, J., Catto, J. L., Hawcroft, M. K., Tan, M. L., Hodges, K. I., and Haywood, J. M.: Borneo Vortices in a warmer climate, Climate and
370   Atmospheric Science, 6, 2, https://doi.org/10.1038/s41612-023-00326-1, 2023.

Muntean, M., Janssens-Maenhout, G., Song, S., Giang, A., Selin, N. E., Zhong, H., Zhao, Y., Olivier, J. G. J., Guizzardi, D., Crippa,
M., Schaaf, E., and Dentener, F.: Evaluating EDGARv4.tox2 speciated mercury emissions ex-post scenarios and their impacts on mod-
elled global and regional wet deposition patterns, Atmospheric Environment, 184, 56–68, https://doi.org/10.1016/j.atmosenv.2018.04.017,
2018.

375   Méndez-López, M., Parente-Sendín, A., Calvo-Portela, N., Gómez-Armesto, A., Eimil-Fraga, C., Alonso-Vega, F., Arias-Estévez, M., and
Nóvoa-Muñoz, J. C.: Mercury in a birch forest in SW Europe: Deposition flux by litterfall and pools in aboveground tree biomass and
soils, Science of The Total Environment, 856, 158 937, https://doi.org/10.1016/j.scitotenv.2022.158937, 2023.

National Centers for Environmental Prediction, National Weather Service, NOAA, U.S. Department of Commerce: NCEP FNL Operational
Model Global Tropospheric Analyses, continuing from July 1999, https://doi.org/10.5065/D6M043C6, last access: 20 March 2024, 2000.

380   NOAA National Geophysical Data Center: ETOPO1 1 Arc-Minute Global Relief Model, Tech. rep., NOAA National Centers for Envi-
ronmental Information, https://www.ncei.noaa.gov/access/metadata/landing-page/bin/iso?id=gov.noaa.ngdc.mgg.dem:316, last access: 20
March 2024, 2009.

Obrist, D., Roy, E. M., Harrison, J. L., Kwong, C. F., Munger, J. W., Moosmüller, H., Romero, C. D., Sun, S., Zhou, J., and Commane,
R.: Previously unaccounted atmospheric mercury deposition in a midlatitude deciduous forest, Proceedings of the National Academy of
385   Sciences, 118, e2105477 118, https://doi.org/10.1073/pnas.2105477118, 2021.

Potapov, P., Li, X., Hernandez-Serna, A., Tyukavina, A., Hansen, M. C., Kommareddy, A., Pickens, A., Turubanova, S., Tang, H., Silva, C. E., Armston, J., Dubayah, R., Blair, J. B., and Hofton, M.: Mapping global forest canopy height through integration of GEDI and Landsat data, Remote Sensing of Environment, 253, 112 165, https://doi.org/10.1016/j.rse.2020.112165, 2021.

Risch, M. R. and Kenski, D. M.: Spatial Patterns and Temporal Changes in Atmospheric-Mercury Deposition for the Midwestern USA, 390   2001–2016, Atmosphere, 9, https://doi.org/10.3390/atmos9010029, 2018.

Saiz-Lopez, A., Acuña, A. U., Trabelsi, T., Carmona-García, J., Dávalos, J. Z., Rivero, D., Cuevas, C. A., Kinnison, D. E., Sitkiewicz, S. P., Roca-Sanjuán, D., and Francisco, J. S.: Gas-Phase Photolysis of Hg(I) Radical Species: A New Atmospheric Mercury Reduction Process, J. Am. Chem. Soc., 141, 8698–8702, https://doi.org/10.1021/jacs.9b02890, 2019.

Sakata, M. and Asakura, K.: Estimating contribution of precipitation scavenging of atmospheric particulate mercury to mercury wet deposi-
395   tion in Japan, Atmospheric Environment, 41, 1669–1680, https://www.sciencedirect.com/science/article/pii/S135223100601051X, 2007.

Salzmann, M.: WRF-Chem/KPP Coupler (WKC) for WRFV3 Users' and Developers' Guide v2.0, Tech. rep., Max Planck Institute for Chemistry, Department of Atmospheric Chemistry, Mainz, Germany, 2008.

Salzmann, M. and Lawrence, M. G.: Automatic Coding of Chemistry Solvers in WRF-CHEM using KPP, in: Papers Presented at the 7th WRF Users' Workshop, National Center for Atmospheric ResearchJune 19-22, 2006, http://www2.mmm.ucar.edu/wrf/users/workshops/
400   WS2006/abstracts/Session06/6_4_Salzmann.pdf, last access: 20 March 2024, 2006.

Sandu, A. and Sander, R.: Technical note: Simulating chemical systems in Fortran90 and Matlab with the Kinetic PreProcessor KPP-2.1, Atmospheric Chemistry and Physics, 6, 187–195, http://www.atmos-chem-phys.net/6/187/2006/acp-6-187-2006.pdf, 2006.

Seo, Y.-S., Han, Y.-J., Choi, H.-D., Holsen, T. M., and Yi, S.-M.: Characteristics of total mercury (TM) wet deposition: Scavenging of atmospheric mercury species, Atmospheric Environment, 49, 69–76, https://doi.org/10.1016/j.atmosenv.2011.12.031, 2012.

405   Shah, V., Jacob, D. J., Thackray, C. P., Wang, X., Sunderland, E. M., Dibble, T. S., Saiz-Lopez, A., Černušák, I., Kellö, V., Castro, P. J., Wu, R., and Wang, C.: Improved Mechanistic Model of the Atmospheric Redox Chemistry of Mercury, Environ. Sci. Technol., 55, 14 445–14 456, https://doi.org/10.1021/acs.est.1c03160, 2021.

Skamarock, W. C., Klemp, J. B., Dudhia, J., Gill, D. O., Liu, Z., Berner, J., Wang, W., Powers, J. G., Duda, M. G., Barker, D. M., and X.-Y, H.: A Description of the Advanced Research WRF Model Version 4.3, Tech. rep., UCAR/NCAR, https://doi.org/10.5065/1DFH-6P97,
410   last access: 20 March 2024, 2019.

Sonke, J. E., Angot, H., Zhang, Y., Poulain, A., Björn, E., and Schartup, A.: Global change effects on biogeochemical mercury cycling, Ambio, 52, 853–876, https://doi.org/10.1007/s13280-023-01855-y, 2023.

Tsui, M. T.-K., Blum, J. D., and Kwon, S. Y.: Review of stable mercury isotopes in ecology and biogeochemistry, Science of The Total Environment, 716, 135 386, https://doi.org/10.1016/j.scitotenv.2019.135386, 2020.

415   UN-Environment: Global Mercury Assessment 2018, Tech. rep., United Nations Environment Programme, https://www.unenvironment.org/resources/publication/global-mercury-assessment-2018, last access: 20 March 2024, 2019.

United Nations: Mnamata Convention on Mercury (2023). Minamata Convention on Mercury: text and annexes., https://minamataconvention.org/sites/default/files/documents/information_document/Minamata-Convention-booklet-Oct2023-EN.pdf, last access: 20 March 2024, 2023.

420   Wang, X., Bao, Z., Lin, C.-J., Yuan, W., and Feng, X.: Assessment of global mercury deposition through litterfall., Environmental Science & Technology, 50, 8548–8557, https://doi.org/10.1021/acs.est.5b06351, 2016.

Wang, X., Yuan, W., Lin, C.-J., and Feng, X.: Mercury cycling and isotopic fractionation in global forests, Critical Reviews in Environmental Science and Technology, 52, 3763–3786, https://doi.org/10.1080/10643389.2021.1961505, 2022.

Wohlgemuth, L., Rautio, P., Ahrends, B., Russ, A., Vesterdal, L., Waldner, P., Timmermann, V., Eickenscheidt, N., Fürst, A., Greve, M.,
425   Roskams, P., Thimonier, A., Nicolas, M., Kowalska, A., Ingerslev, M., Merilä, P., Benham, S., Iacoban, C., Hoch, G., Alewell, C.,
and Jiskra, M.: Physiological and climate controls on foliar mercury uptake by European tree species, Biogeosciences, 19, 1335–1353,
https://doi.org/10.5194/bg-19-1335-2022, 2022.

Wright, L. P., Zhang, L., and Marsik, F. J.: Overview of mercury dry deposition, litterfall, and throughfall studies, Atmospheric Chemistry
and Physics, 16, 13 399–13 416, https://doi.org/10.5194/acp-16-13399-2016, 2016.

430   Yuan, T., Zhang, P., Song, Z., Huang, S., Wang, X., and Zhang, Y.: Buffering effect of global vegetation on the air-land exchange
of mercury: Insights from a novel terrestrial mercury model based on CESM2-CLM5, Environment International, 174, 107 904,
https://doi.org/10.1016/j.envint.2023.107904, 2023.

Zhou, H., Zhou, C., Hopke, P. K., and Holsen, T. M.: Mercury wet deposition and speciated mercury air concentrations at rural and urban
sites across New York state: Temporal patterns, sources and scavenging coefficients., The Science of the Total Environment, 637-638,
435   943–953, https://doi.org/10.1016/j.scitotenv.2018.05.047, 2018a.

Zhou, J. and Obrist, D.: Global mercury assimilation by vegetation., Environmental Science and Technology, 55, 14 245–14 257,
https://doi.org/10.1021/acs.est.1c03530, 2021.

Zhou, J., Wang, Z., and Zhang, X.: Deposition and Fate of Mercury in Litterfall, Litter, and Soil in Coniferous and Broad-Leaved Forests, J.
Geophys. Res. Biogeosci., 123, 2590–2603, https://doi.org/10.1029/2018JG004415, 2018b.

440   Zhou, J., Obrist, D., Dastoor, A., Jiskra, M., and Ryjkov, A.: Vegetation uptake of mercury and impacts on global cycling, Nature Reviews
Earth and Environment, 2, 269–284, https://doi.org/10.1038/s43017-021-00146-y, 2021.

Table 1. Hg^0 deposition velocity ($cm\,s^{-1}$) as a function of Leaf Area Index

Leaf Area Index	Vegetation Uptake Rate	Deposition Velocity $cm\,s^{-1}$
2	Slow	0.013
	Fast	0.038
4	Slow	0.026
	Fast	0.075
6	Slow	0.052
	Fast	0.11
8	Slow	0.052
	Fast	0.15

Table 2. Fraction of annual emissions deposited within the modelling domain: Africa

italics: < 10%, **bold:** > 25%, †:convective deposition exceeds foliar uptake, ‡:dry/wet depostion ratio ≤1

Location	Oxidation Rate	Foliar Uptake	Deposition in domain (%)	Deposition to vegetation (%)	Dry deposition of Hg^{II} (%)	Convective deposition (%)	Non-convective deposition (%)	Dry/Wet Deposition ratio	Convective / Non-convective Deposition ratio
Ghana	Fast	Slow	14.69	7.29	1.99	5.29	0.12	1.72	44.03
	Slow	Slow	11.26	7.38	1.05	2.77	0.06	2.98	43.42
	Fast	Fast	24.59	18.10	1.74	4.64	0.10	4.18	44.32
	Slow	Fast	21.70	18.31	0.92	2.42	0.06	7.75	43.74
Senegal	Fast	Slow	11.54	4.13†	2.42	4.87†	0.13	1.31	37.81
	Slow	Slow	*8.10*	4.23	1.26	2.54	0.07	2.11	37.30
	Fast	Fast	17.56	10.44	2.30	4.69	0.12	2.65	38.38
	Slow	Fast	14.40	10.69	1.20	2.44	0.06	4.75	37.87
Burkina Faso	Fast	Slow	13.88	4.06†	2.86	6.81†	0.16	0.99‡	43.22
	Slow	Slow	*9.32*	4.18	1.50	3.56	0.08	1.56	42.59
	Fast	Fast	19.92	10.49	2.73	6.56	0.15	1.97	43.71
	Slow	Fast	15.71	10.77	1.43	3.42	0.08	3.48	43.08
Sudan	Fast	Slow	12.13	3.37†	2.69	5.92†	0.15	1.00‡	39.14
	Slow	Slow	*8.11*	3.51	1.42	3.10	0.08	1.55	38.70
	Fast	Fast	16.77	8.39	2.56	5.68	0.14	1.88	39.55
	Slow	Fast	13.11	8.71	1.35	2.97	0.08	3.30	39.13
Lake Victoria	Fast	Slow	12.14	6.11	2.02	3.87	0.13	2.03	29.17
	Slow	Slow	*9.39*	6.23	1.06	2.03	0.07	3.48	29.09
	Fast	Fast	20.33	14.92	1.80	3.48	0.12	4.64	29.36
	Slow	Fast	18.01	15.18	0.95	1.82	0.06	8.56	29.29

Table 3. Fraction of annual emissions deposited within the modelling domain: SE Asia

italics: < 10%, **bold**: > 25%, †:convective deposition exceeds foliar uptake, ‡:dry/wet depostion ratio ≤1

Location	Oxidation Rate	Foliar Uptake	Deposition in domain (%)	Deposition to vegetation (%)	Dry deposition of Hg^{II} (%)	Convective deposition (%)	Non-convective deposition (%)	Dry/Wet Deposition ratio	Convective / Non-convective Deposition ratio
Mekong	Fast	Slow	15.39	7.00	2.17	5.95	0.27	1.48	22.34
	Slow	Slow	11.50	7.07	1.13	3.16	0.14	2.49	22.72
	Fast	Fast	**25.12**	17.52	1.96	5.40	0.24	3.46	22.58
	Slow	Fast	21.69	17.69	1.02	2.86	0.12	6.26	22.96
Sumatra	Fast	Slow	14.14	5.18†	1.35	7.47†	0.15	0.86‡	50.90
	Slow	Slow	*9.95*	5.22	0.70	3.95	0.08	1.47	50.63
	Fast	Fast	21.56	13.28	1.24	6.91	0.13	2.06	51.40
	Slow	Fast	17.74	13.37	0.65	3.65	0.07	3.76	51.12
Kalimantan	Fast	Slow	**35.52**	23.33	4.99	7.01	0.18	3.94	38.94
	Slow	Slow	**29.72**	23.40	2.53	3.70	0.09	6.83	39.12
	Fast	Fast	**78.35**	66.31	4.97	6.89	0.18	10.09	39.07
	Slow	Fast	**72.74**	66.50	2.51	3.63	0.09	18.53	39.25
Papua New Guinea	Fast	Slow	14.35	5.81†	1.62	6.70†	0.21	1.07	31.23
	Slow	Slow	10.25	5.83	0.82	3.49	0.11	1.85	31.73
	Fast	Fast	24.87	16.42	1.61	6.63	0.21	2.63	31.18
	Slow	Fast	20.83	16.45	0.82	3.45	0.11	4.85	31.68

Table 4. Fraction of annual emissions deposited within the modelling domain: South America

italics: < 10%, **bold**: > 25%, †:convective deposition exceeds foliar uptake, ‡:dry/wet deposition ratio ≤1

Location	Oxidation Rate	Foliar Uptake	Deposition in domain (%)	Deposition to vegetation (%)	Dry deposition of Hg^{II} (%)	Convective deposition (%)	Non-convective deposition (%)	Dry/Wet Deposition ratio	Convective / Non-convective Deposition ratio
Bolivia	Fast	Slow	*7.47*	3.73	1.56	1.98	0.20	2.42	9.91
	Slow	Slow	*5.73*	3.78	0.81	1.04	0.10	4.03	10.00
	Fast	Fast	12.94	9.47	1.44	1.85	0.18	5.37	10.01
	Slow	Fast	11.40	9.59	0.75	0.96	0.10	9.76	10.10
Columbia	Fast	Slow	8.25	3.44‡	1.05	3.65‡	0.12	1.19	31.37
	Slow	Slow	*5.96*	3.47	0.55	1.88	0.06	2.07	31.06
	Fast	Fast	13.31	8.81	0.97	3.42	0.11	2.78	31.47
	Slow	Fast	11.20	8.87	0.51	1.76	0.06	5.15	31.15
Brazil	Fast	Slow	*8.49*	5.22	1.44	1.50	0.33	3.63	4.54
	Slow	Slow	*6.98*	5.28	0.74	0.78	0.17	6.34	4.62
	Fast	Fast	16.27	13.28	1.31	1.38	0.30	8.68	4.55
	Slow	Fast	14.97	13.42	0.68	0.72	0.15	16.20	4.63
Guyana	Fast	Slow	14.15	9.85	1.41	2.81	0.09	3.89	30.78
	Slow	Slow	12.14	9.90	0.73	1.46	0.05	7.06	30.44
	Fast	Fast	**26.23**	22.68	1.15	2.31	0.07	9.98	31.13
	Slow	Fast	**24.64**	22.80	0.60	1.20	0.04	18.87	30.79

Table 5. Percentage of in-domain deposition versus distance from the centre of the small domain cell containing the emissions for the four deposition pathways, v_d=1cm s^{-1}

Emission Source	Deposition type	Deposition Distance from source, km						
		0 - 250	250 - 500	500 - 1000	1000 - 2000	2000 - 5000	5000 - 10000	> 10000
Burkina Faso	Foliar uptake	24	21	10	9	3	32	2
	Dry deposition	2	4	7	10	33	32	12
	Conv. precip.	<1	<1	1	5	30	55	8
	Non-conv. precip.	<1	<1	2	4	31	49	13
Senegal	Foliar uptake	37	10	3	<1	7	42	<1
	Dry deposition	2	3	6	12	35	35	8
	Conv. precip.	<1	<1	2	6	42	45	4
	Non-conv. precip.	<1	<1	1	4	32	54	8
Ghana	Foliar uptake	64	11	8	4	2	10	<1
	Dry deposition	3	5	10	12	29	29	13
	Conv. precip.	<1	2	5	7	34	44	7
	Non-conv. precip.	7	3	5	5	19	47	14
Sudan	Foliar uptake	12	4	12	20	24	8	20
	Dry deposition	1	2	6	13	28	28	22
	Conv. precip.	<1	<1	1	3	23	51	21
	Non-conv. precip.	<1	<1	2	12	25	31	29
Lake Victoria	Foliar uptake	43	15	13	13	4	5	8
	Dry deposition	3	3	6	12	24	3	20
	Conv. precip.	<1	<1	5	14	18	43	19
	Non-conv. precip.	4	5	13	13	14	28	24

Figure 1. The three supra-continental domains and the nested domains used in this study

(a) Africa
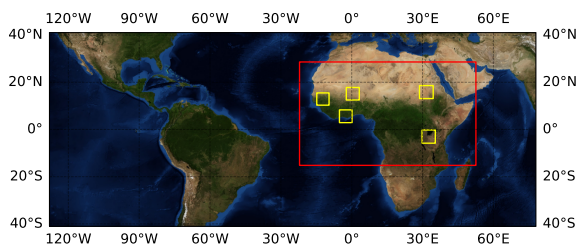
(b) South-East Asia
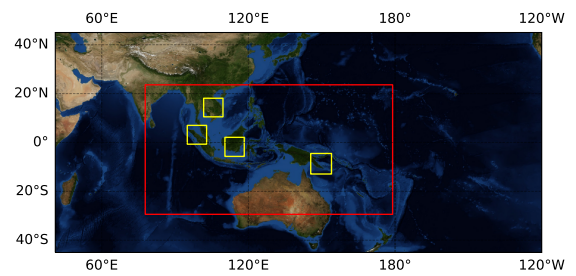
(c) South America
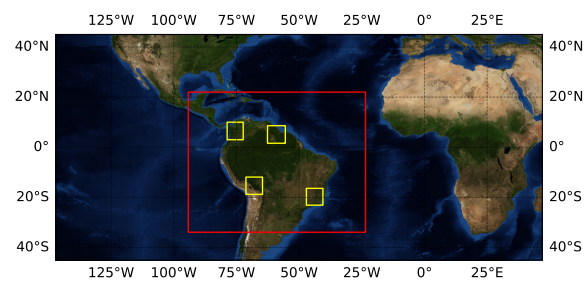
Figure 2. Emissions and relief of the South American Domains, emissions in $\mathrm{mol\,km^{-2}\,hr^{-1}}$
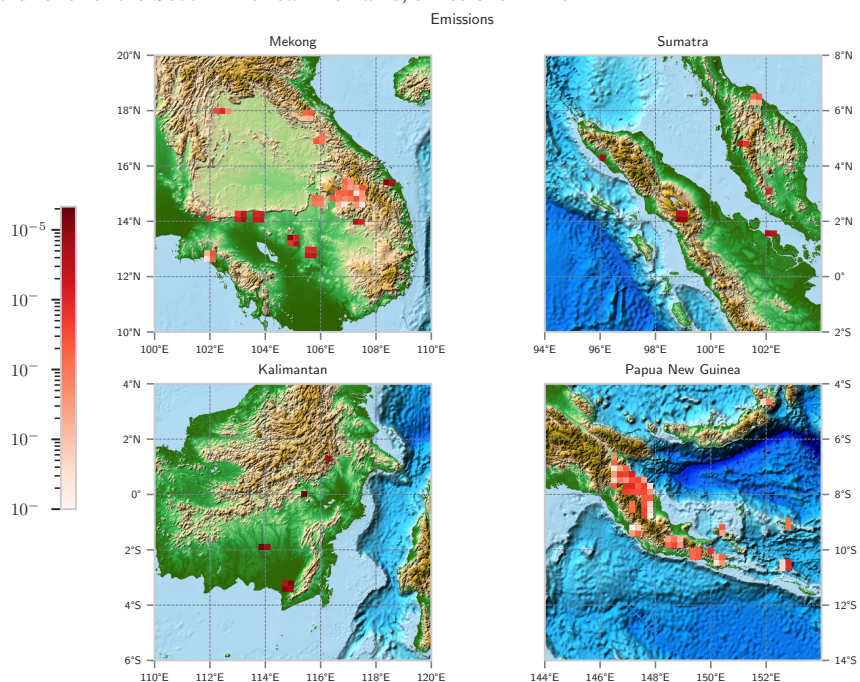
Figure 3. Normalised Hg Deposition vs. distance from emission source for the South American domains. The left colour bar represents deposition to land, the right to seas and oceans

(a) Bolivia

(b) Columbia

(c) Brazil

(d) Guyana
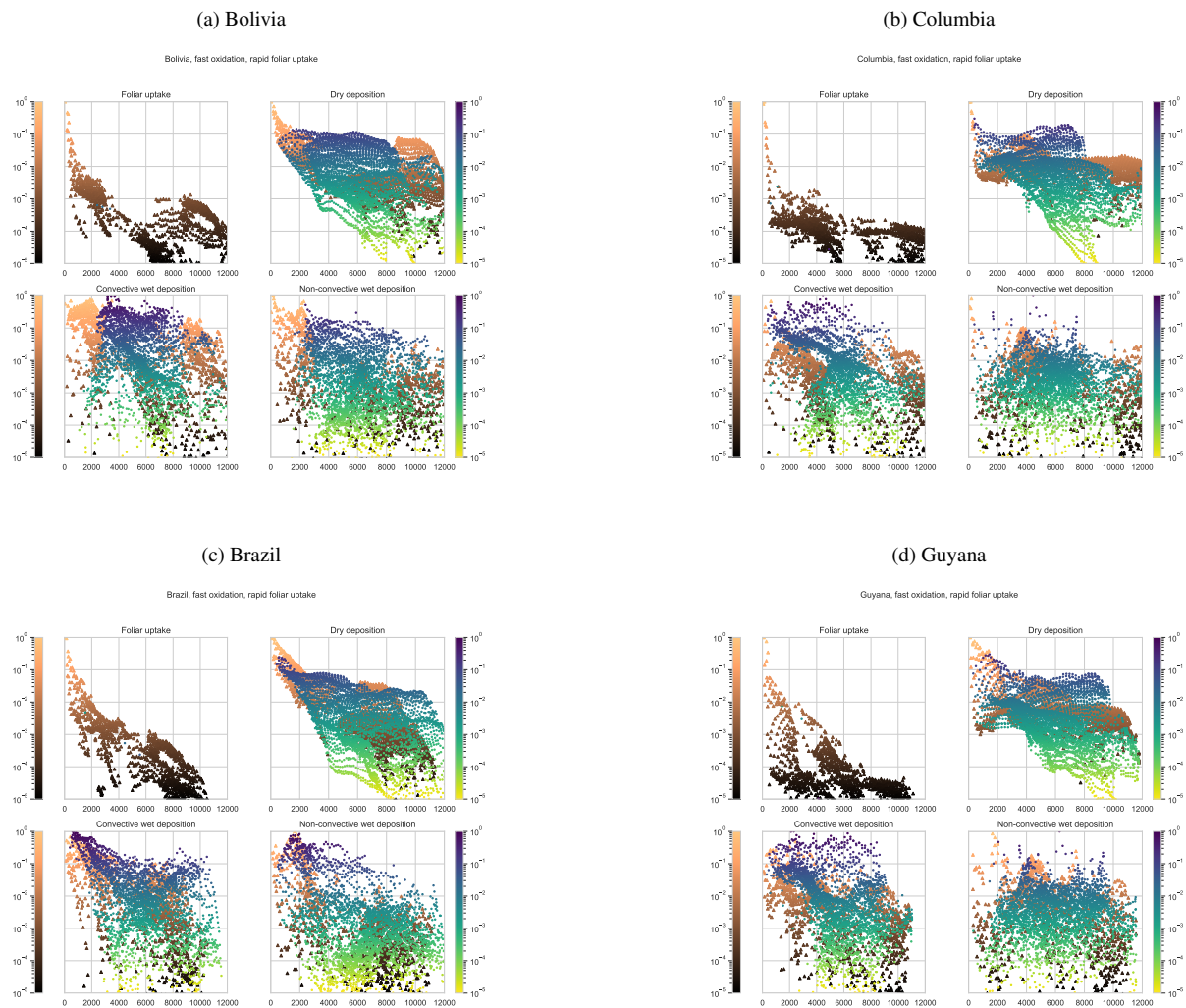
Figure 4. Normalised Hg Deposition vs. distance from emission source for the South-East Asian domains. The left colour bar represents deposition to land, the right to seas and oceans

(a) Mekong

(b) Sumatra

(c) Kalimantan

(d) Papua New Guinea
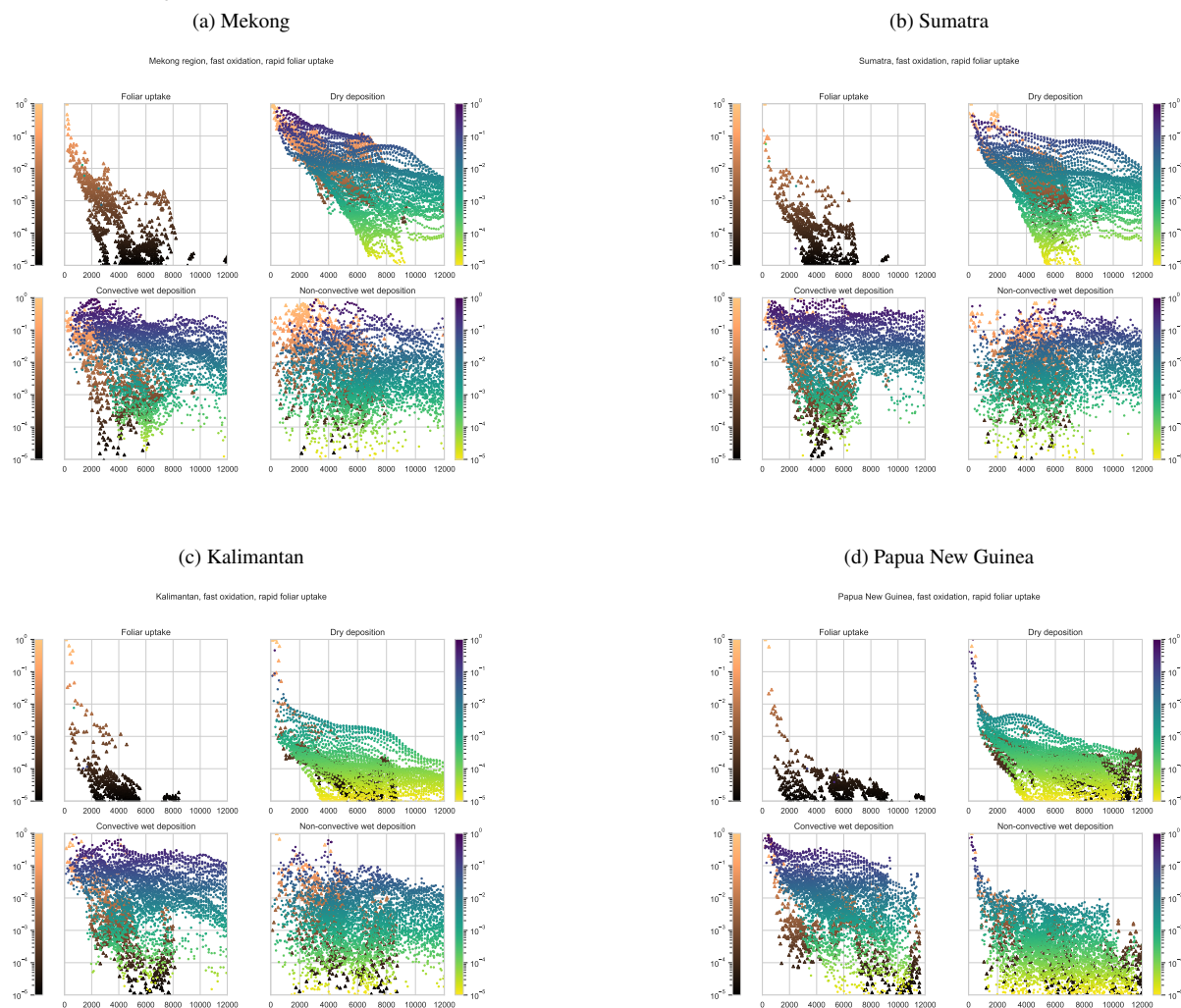
Figure 5. Normalised Hg Deposition vs. distance from emission source for the African domains. The left colour bar represents deposition to land, the right to seas and oceans

(a) Ghana

(b) Burkina Faso

(c) Senegal

(d) Sudan

(e) Lake Victoria
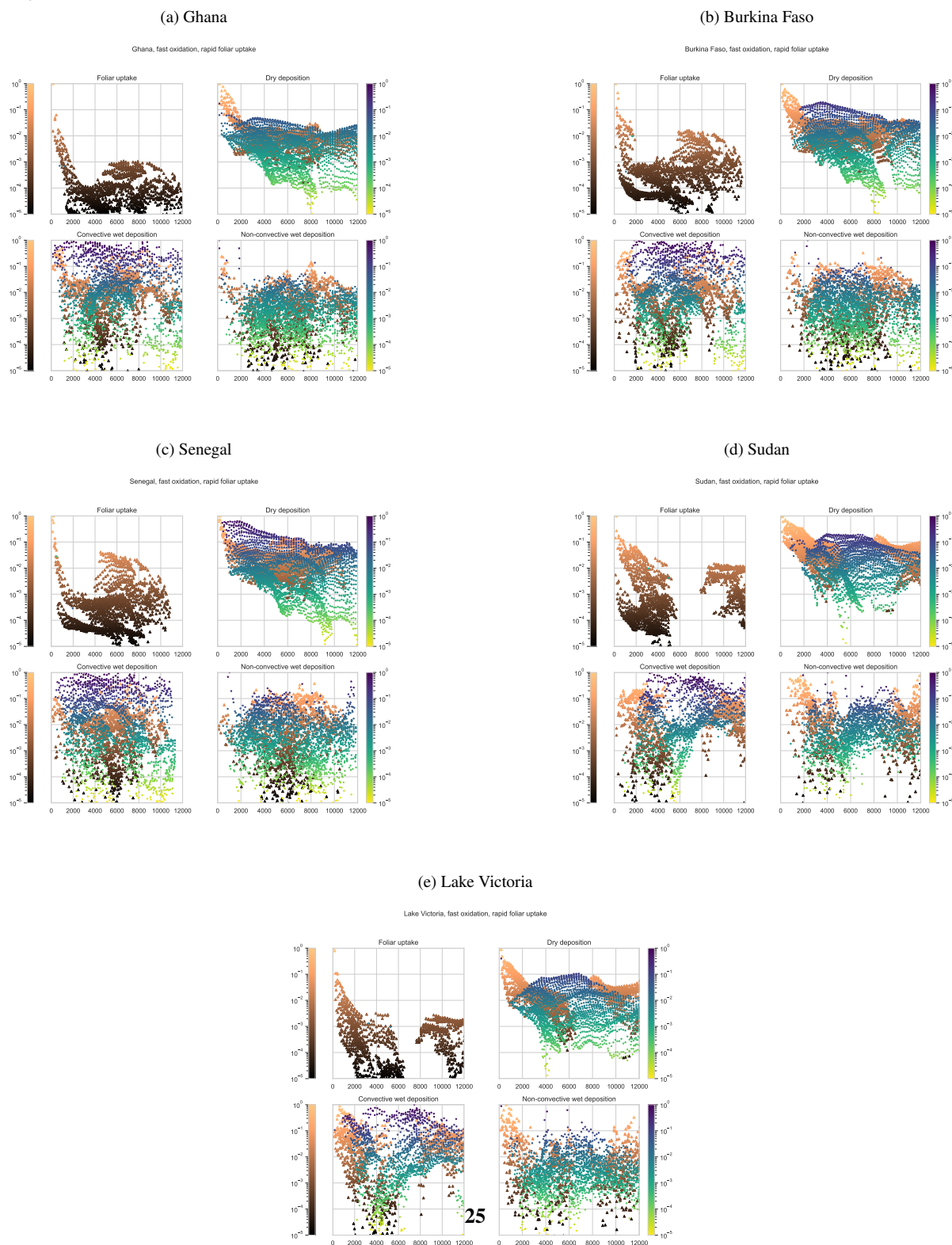
Figure 6. Deposition vs. distance, South-East Asian emission domains. Percentages of within domain deposition for each deposition pathway
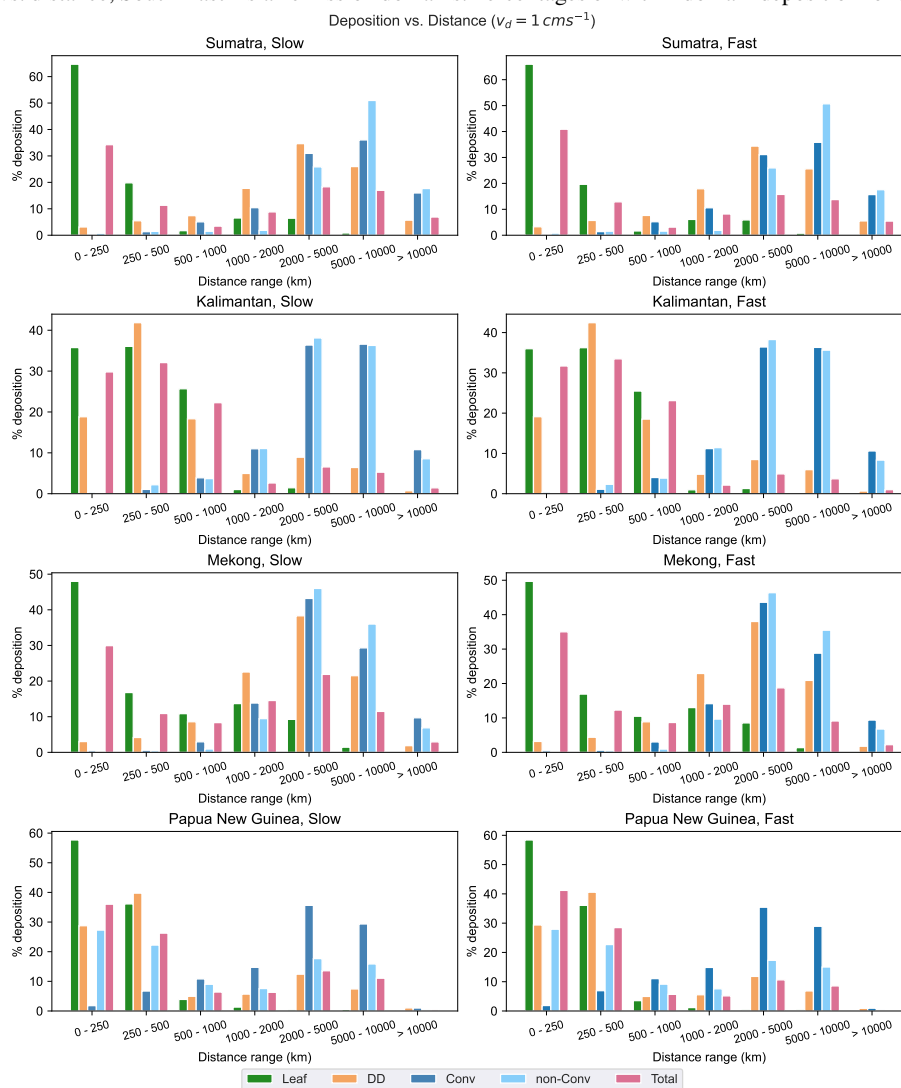
Figure 7. Deposition vs. distance, South American emission domains. Percentages of within domain deposition for each deposition pathway
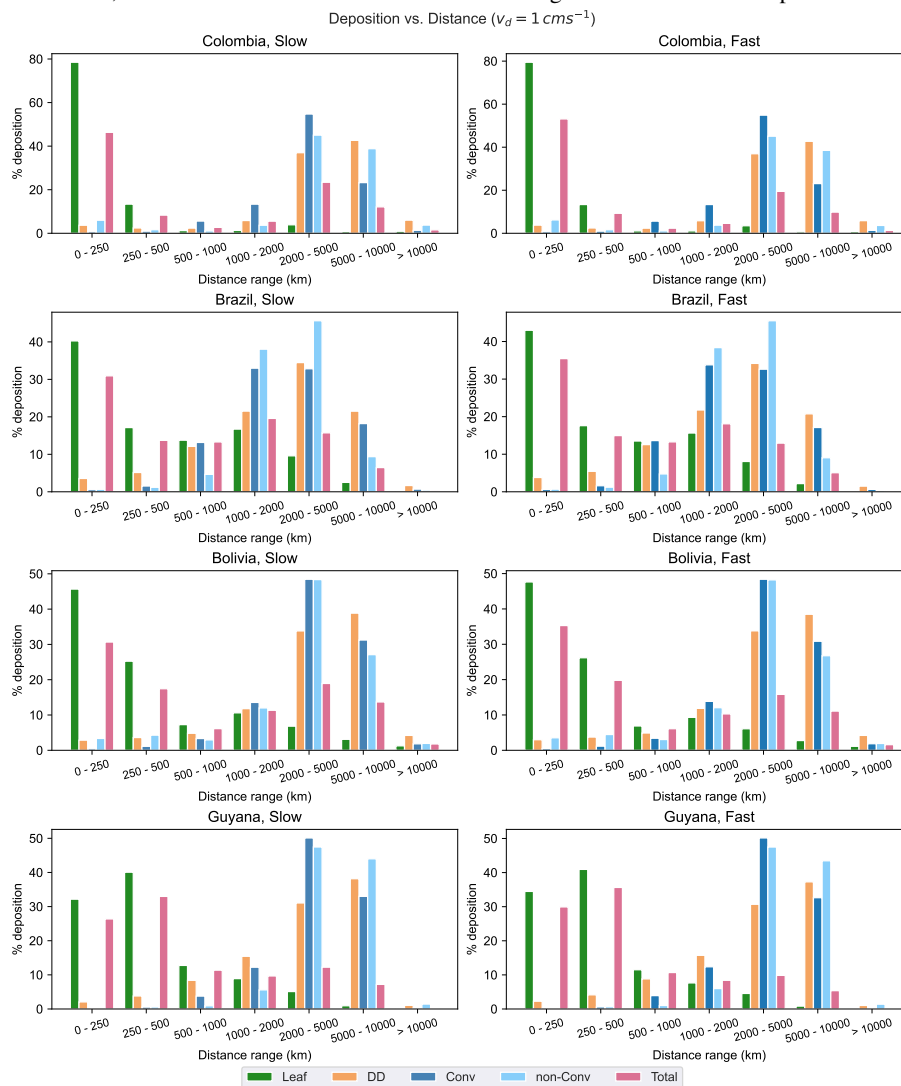
Figure 8. Normalised Hg deposition from the domain in Senegal
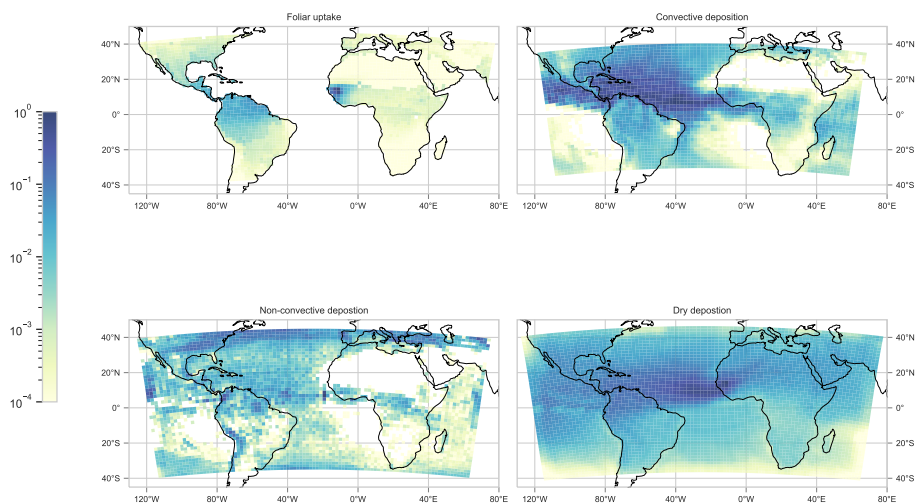
Figure 9. Deposition vs. distance, African emission domains. Percentages of within domain deposition for each deposition pathway
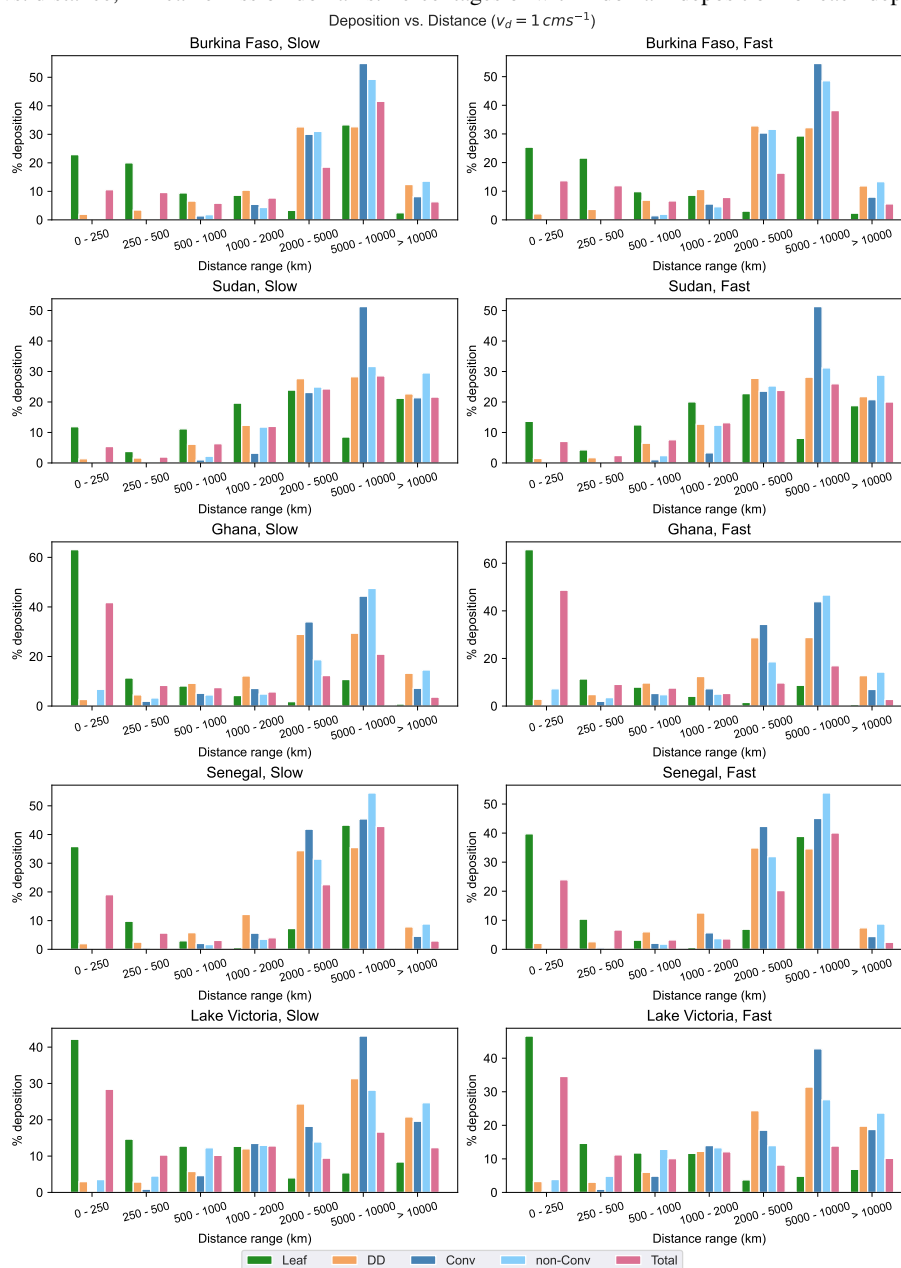
Appendix A: The difference due to the dry deposition velocity of $Hg^{II}_{(g)}$

Table A1. Difference in deposition due to v_d, African domains (the deposition percentages are referred to each emission domain total)

Location	Oxidation Rate	Foliar Uptake	In Domain Deposition (%) ($v_d = 1\,\mathrm{cm\,s^{-1}}$)	Hg^{II} Dry Deposition (%) ($v_d = 1\,\mathrm{cm\,s^{-1}}$)	In Domain Deposition (%) ($v_d = 2\,\mathrm{cm\,s^{-1}}$)	Hg^{II} Dry Deposition(%) ($v_d = 2\,\mathrm{cm\,s^{-1}}$)	Hg^{II} Dry Deposition Increase (%)	In Domain Deposition Increase (%)
Ghana	Fast	Slow	14.69	1.99	15.52	3.06	53.25	5.60
	Slow	Slow	11.26	1.05	11.69	1.61	53.23	3.83
	Fast	Fast	24.59	1.74	25.30	2.67	53.22	2.88
	Slow	Fast	21.70	0.92	22.07	1.41	53.20	1.68
Senegal	Fast	Slow	11.54	2.42	12.58	3.68	52.42	8.94
	Slow	Slow	8.10	1.26	8.64	1.92	52.43	6.65
	Fast	Fast	17.56	2.30	18.54	3.51	52.41	5.59
	Slow	Fast	14.40	1.20	14.91	1.83	52.42	3.55
Burkina Faso	Fast	Slow	13.88	2.86	15.10	4.36	52.66	8.78
	Slow	Slow	9.32	1.50	9.96	2.29	52.64	6.88
	Fast	Fast	19.92	2.73	21.08	4.16	52.65	5.83
	Slow	Fast	15.71	1.43	16.32	2.19	52.64	3.88
Sudan	Fast	Slow	12.13	2.69	13.27	4.10	52.45	9.41
	Slow	Slow	8.11	1.42	8.71	2.16	52.44	7.44
	Fast	Fast	16.77	2.56	17.85	3.90	52.46	6.48
	Slow	Fast	13.11	1.35	13.68	2.06	52.45	4.38
Lake Victoria	Fast	Slow	12.14	2.02	12.97	3.12	54.34	6.83
	Slow	Slow	9.39	1.06	9.82	1.64	54.35	4.55
	Fast	Fast	20.33	1.80	21.04	2.78	54.18	3.53
	Slow	Fast	18.01	0.95	18.37	1.46	54.18	1.98

Table A2. Difference in deposition due to v_d, South American domains (the deposition percentages are referred to each emission domain total)

Location	Oxidation Rate	Foliar Uptake	In Domain Deposition (%) ($v_d = 1\,\mathrm{cm\,s^{-1}}$)	Hg^{II} Dry Deposition (%)	In Domain Deposition (%) ($v_d = 2\,\mathrm{cm\,s^{-1}}$)	Hg^{II} Dry Deposition(%)	Hg^{II} Dry Deposition Increase (%)	In Domain Deposition Increase (%)
Bolivia	Fast	Slow	7.47	1.56	8.13	2.34	50.06	8.85
	Slow	Slow	5.73	0.81	6.07	1.22	50.06	5.96
	Fast	Fast	12.94	1.44	13.54	2.16	50.07	4.66
	Slow	Fast	11.40	0.75	11.70	1.13	50.07	2.69
Columbia	Fast	Slow	8.25	1.05	8.72	1.59	52.06	5.62
	Slow	Slow	5.96	0.55	6.20	0.83	52.07	4.03
	Fast	Fast	13.31	0.97	13.73	1.48	52.08	3.19
	Slow	Fast	11.20	0.51	11.41	0.77	52.09	1.92
Brazil	Fast	Slow	8.49	1.44	9.08	2.16	50.01	6.90
	Slow	Slow	6.98	0.74	7.28	1.12	50.01	4.24
	Fast	Fast	16.27	1.31	16.79	1.97	50.04	3.15
	Slow	Fast	14.97	0.68	15.22	1.02	50.04	1.64
Guyana	Fast	Slow	14.15	1.41	14.76	2.14	51.74	4.26
	Slow	Slow	12.14	0.73	12.45	1.11	51.75	2.55
	Fast	Fast	26.23	1.15	26.71	1.75	51.78	1.84
	Slow	Fast	24.64	0.60	24.88	0.91	51.79	0.99

Table A3. Difference in deposition due to v_d, South-East Asian domains (the deposition percentages are referred to each emission domain total)

Location	Oxidation Rate	Foliar Uptake	In Domain Deposition (%) ($v_d = 1\,\mathrm{cm\,s^{-1}}$)	Hg^{II} Dry Deposition (%) ($v_d = 1\,\mathrm{cm\,s^{-1}}$)	In Domain Deposition (%) ($v_d = 2\,\mathrm{cm\,s^{-1}}$)	Hg^{II} Dry Deposition(%) ($v_d = 2\,\mathrm{cm\,s^{-1}}$)	Hg^{II} Dry Deposition Increase (%)	In Domain Deposition Increase (%)
Mekong	Fast	Slow	15.39	2.17	17.34	4.52	107.77	12.61
	Slow	Slow	11.50	1.13	12.51	2.35	107.82	8.82
	Fast	Fast	25.12	1.96	26.87	4.06	107.67	7.00
	Slow	Fast	21.69	1.02	22.61	2.11	107.72	4.26
Sumatra	Fast	Slow	14.14	1.35	15.44	2.92	116.90	9.17
	Slow	Slow	9.95	0.70	10.64	1.53	116.70	6.88
	Fast	Fast	21.56	1.24	22.77	2.68	116.79	5.59
	Slow	Fast	17.74	0.65	18.39	1.40	116.59	3.63
Kalimantan	Fast	Slow	35.52	4.99	43.02	12.79	156.05	21.12
	Slow	Slow	29.72	2.53	33.53	6.46	155.61	12.80
	Fast	Fast	78.35	4.97	85.90	12.73	156.23	9.64
	Slow	Fast	72.74	2.51	76.61	6.43	155.80	5.32
Papua New Guinea	Fast	Slow	14.35	1.62	16.84	4.23	161.55	17.41
	Slow	Slow	10.25	0.82	11.52	2.15	160.70	12.42
	Fast	Fast	24.87	1.61	27.39	4.21	161.76	10.14
	Slow	Fast	20.83	0.82	22.13	2.14	160.91	6.25

Appendix B: Code changes and additions

B1   Registry and KPP

445 In the description below 'asgm' is used to denote a generic ASGM emission region. If more than one region is used in the simulation, as in this study, 'asgm' needs to be replaced with a domain identifier and all the species from each domain include in the definitions of the chemical, emission and deposition mechanisms. A new mechanism needs to be included in the /WRF/chem/KPP/mechanisms folder. This requires a .eqn file which includes the reactions;

#EQUATIONS

450 *(1) Hg_180_slo_asgm=HgII_180_slo_asgm : 6.430D-8 ; (1./(180*86400)*

*(2) Hg_270_slo_asgm=HgII_270_slo_asgm : 4.286D-8 ; (1./(270*86400)*

*(3) Hg_360_slo_asgm=HgII_360_slo_asgm : 3.215D-8 ; (1./(360*86400)*

*(4) Hg_180_mid_asgm=HgII_180_mid_asgm : 6.430D-8 ; (1./(180*86400)*

*(5) Hg_270_mid_asgm=HgII_270_mid_asgm : 4.286D-8 ; (1./(270*86400)*

455 *(6) Hg_360_mid_asgm=HgII_360_mid_asgm : 3.215D-8 ; (1./(360*86400)*

*(7) Hg_180_hi_asgm=HgII_180_hi_asgm : 6.430D-8 ; (1./(180*86400)*

*(8) Hg_270_hi_asgm=HgII_270_hi_asgm : 4.286D-8 ; (1./(270*86400)*

*(9) Hg_360_hi_asgm=HgII_360_hi_asgm : 3.215D-8 ; (1./(360*86400)*

460   and a .spc file including the chemical species

#DEFVAR

Hg_180_slo_asgm =IGNORE ;

HgII_180_slo_asgm =IGNORE ;

Hg_270_slo_asgm =IGNORE ;

465 *HgII_270_slo_asgm =IGNORE ;*

Hg_360_slo_asgm =IGNORE ;

HgII_360_slo_asgm =IGNORE ;

Hg_180_mid_asgm =IGNORE ;

HgII_180_mid_asgm =IGNORE ;

470 *Hg_270_mid_asgm =IGNORE ;*

HgII_270_mid_asgm =IGNORE ;

Hg_360_mid_asgm =IGNORE ;

HgII_360_mid_asgm =IGNORE ;

Hg_180_hi_asgm =IGNORE ;

475 *HgII_180_hi_asgm =IGNORE ;*

Hg_270_hi_asgm =IGNORE ;

HgII_270_hi_asgm =IGNORE ;

Hg_360_hi_asgm =IGNORE ;

HgII_360_hi_asgm =IGNORE ;

480   where 180, 270, and 360 refer to the oxidation rate, lo,mid and hi to the foliar uptake rate. The species, species emission, and chemical mechanism and emission packages need to added to the file registry.chem in WRF/Registry, e.g.

state real hg_180_slo_asgm ikjftb chem 1 - i8rh02usdf=(bdy_interp:dt) "HG_180_SLO_ASGM" "HG 6mon SLO ASGM" "ppmv"

state real hgii_180_slo_asgm ikjftb chem 1 - i8rh02usdf=(bdy_interp:dt) "HGII_180_SLO_ASGM" "HGII 6mon SLO ASGM" "ppmv"

etc defines the species,

485   *state real e_hg_180_slo_asgm i+jf emis_ant 1 Z i5h "E_HG_180_SLO_ASGM" "EMISSIONS HG_180_SLO_ASGM" "mol km^{-2}hr^{-1}"*

etc defines the species emitted,

package hg_asgm_kpp chem_opt==756 - chem:hg_180_slo_asgm,hgii_180_slo_asgm,hg_270_slo_asgm,hgii_270_slo_asgm,hg_360_slo_asgm,hgii_360_slo_asgm

etc defines the chemical mechanism package and its namelist.input option number,

package e_hg_asgm emiss_opt==36 - emis_ant:e_hg_180_slo_asgm,e_hg_270_slo_asgm,e_hg_360_slo_asgm,

490   etc defines the emissions package and its namelist.input option.

The deposition package is defined similarly, but includes the four possible deposition pathways, hence;

state real hg180_slo_dep_asgm i%jf hg_dep 1 - rh03 "hg180_SLO_dep_ASGM" "Hg 6m SLO deposition ASGM" "-"

state real hg180_slo_cdep_asgm i%jf hg_dep 1 - rh03 "hg180_SLO_cdep_ASGM" "Hg 6m SLO conv deposition ASGM" "-"

state real hg180_slo_ncdep_asgm i%jf hg_dep 1 - rh03 "hg180_SLO_ncdep_ASGM" "Hg 6m SLO non-conv deposition ASGM" "-"

495   *state real hg180_slo_dd_asgm i%jf hg_dep 1 - rh03 "hg180_SLO_dd_ASGM" "Hg 6m SLO dry dep HgII ASGM" "-"*

package Hg_cfpp_dep mercury_tr_dep==1 - Hg_dep:hg180_slo_dep_asgm,hg180_slo_cdep_asgm,hg180_slo_ncdep_asgm,hg180_slo_dd_asgm,

etc, where dep, cdep, ncdep, and dd in the variable names refer to foliar uptake, convective, non-convective and dry deposition respectively. However this is completely new and is not simply an extra option to a namelist entry, therefore the Hg deposition option needs to be added to namelist;

500   *rconfig integer veg_uptake_opt namelist,chem max_domains 1 rh "veg_uptake_opt" "" ""*

rconfig integer mercury_tr_dep namelist,chem max_domains 1 rh "Hg_tracer_deposition" "" ""

where veg_uptake_opt turns the deposition on and off, and mercury_tr_dep is the option to choose the tracer deposition mechanism, which will be different for each emission domain included in the chemical mechanism.

Appropriate changes to include the mechanism as described in the WRF-Chem/KPP Coupler guide (Salzmann, 2008) and

505   in the latest WRF-Chem Users Guide, (https://ruc.noaa.gov/wrf/wrf-chem/model_info.htm), need to be made in

/WRF/share/module_chem_share.F,

/WRF/chem/emissions_driver.F,

/WRF/chem/dry_dep_driver.F,

/WRF/chem/chem_driver.f90,

510   */WRF/chem/emissions_driver.F and*

/WRF/chem/module_input_chem_data.F.